Towards imaging of atmospheric trace gases using Fabry Perot Interferometer Correlation Spectroscopy in the UV and visible spectral range

Jonas Kuhn[1,2], Ulrich Platt[1,2], Nicole Bobrowski[1,2], and Thomas Wagner[2]

[1]Institute of Environmental Physics, University of Heidelberg, Germany
[2]Max Planck Institute for Chemistry, Mainz, Germany

Correspondence: J. Kuhn (jkuhn@iup.uni-heidelberg.de)

Abstract. Many processes in the lower atmosphere including transport, turbulent mixing and chemical conversions happen on time scales of the order of seconds (e.g. at point sources). Remote sensing of atmospheric trace gases in the UV and visible spectral range (UV/Vis) commonly uses dispersive spectroscopy (e.g. Differential Optical Absorption Spectroscopy, DOAS). The recorded spectra allow for the direct identification, separation and quantification of narrow band absorption of trace gases.

5 However, these techniques are typically limited to a single viewing direction and limited by the light throughput of the spectrometer setup. While two dimensional imaging is possible by spatial scanning, the temporal resolution remains poor (often several minutes per image). Therefore, processes on time scales of seconds cannot be directly resolved by state of the art dispersive methods.

We investigate the application of Fabry-Perot Interferometers (FPIs) for the optical remote sensing of atmospheric trace gases

10 in the UV/Vis. By choosing a FPI transmission spectrum, which is optimised to correlate with narrow band (ideally periodic) absorption structures of the target trace gas, column densities of the trace gas can be determined with a sensitivity and selectivity comparable to dispersive spectroscopy, using only a small number of spectral channels (FPI tuning settings). Different from dispersive optical elements, the FPI can be implemented in full frame imaging setups (cameras), which can reach high spatio-temporal resolution. In principle, FPI Correlation Spectroscopy can be applied for any trace gas with distinct absorption

15 structures in the UV/Vis.

We present calculations for the application of FPI Correlation Spectroscopy to SO_2, BrO and NO_2 for exemplary measurement scenarios. Besides high sensitivity and selectivity we find that the spatio temporal resolution of FPI Correlation Spectroscopy can be more than two orders of magnitude higher than state of the art DOAS measurements.

As proof of concept we built a one-pixel prototype implementing the technique for SO_2 in the UV. Good agreement with

20 our calculations and conventional measurement techniques are demonstrated and no cross sensitivities to other trace gases are observed.

1 Introduction

Within the last decades, progress in optical remote sensing of atmospheric trace gases led to a better understanding of many

important processes including air pollution, ozone and halogen chemistry, and the evolution of volcanic plumes. Narrow band

structures in the trace gas molecule's absorption spectrum are used to identify and quantify the amount of a trace gas integrated

5   along a line of sight, i.e. its column density (CD, typically in units of $\mathrm{molec\,cm^{-2}}$) and to separate its absorption signal from

interfering gas absorptions and scattering processes.

Differential Optical Absorption Spectroscopy (DOAS, see Platt and Stutz, 2008, for details) has become a well established

technique for atmospheric trace gas remote sensing in the UV/Vis with high sensitivity (detection limits within the ppb to ppt

range for atmospheric light paths of a few kilometers). A spectrometer and a telescope with narrow field of view (FOV) are used

10   to record spectra $I(\lambda)$ of scattered sunlight, which are compared to a reference spectrum $I_0(\lambda)$. Beer Lambert's law describes

the corresponding spectral optical density $\tau(\lambda)$ with $\sigma_i(\lambda)$ and $c_i(l)$ being the absorption cross section and the concentration

of trace gas species i along a line of sight L, respectively:

$$\tau(\lambda) = -\log\frac{I(\lambda)}{I_0(\lambda)} = \int\limits_0^L \sum_i \sigma_i(\lambda)c_i(l)\mathrm{d}l + \text{scattering at molecules and aerosols} \tag{1}$$

Atmospheric UV/Vis optical densities are dominated by trace gas absorption and scattering processes at air molecules or

15   aerosols. The known absorption cross sections of the trace gases together with a polynomial, which accounts for the broad

band absorption and scattering effects are fitted to the measured spectral optical density. The fit coefficients represent the CDs

$S_i = \int_0^L c_i(l)\mathrm{d}l$, i.e. the integrated trace gas concentration along the light path difference of $I(\lambda)$ and the reference $I_0(\lambda)$. In

principle, spatial distributions of trace gases (images or height profiles) can be recorded by scanning of viewing angles with

a narrow FOV telescope (e.g. Multi-Axis DOAS, Hönninger et al., 2004). More complicated optical setups allow to record

20   spectra of an entire image column at once by using a two dimensional detector array (e.g. Imaging DOAS, Lohberger et al.,

2004). Images can then be recorded by column by column (push broom) scanning. The acquisition times of these techniques

are rather high (often several minutes per image or profile for typical trace gas CDs) limiting their application to processes that

are spatially homogeneous on that time scale or processes with very high trace gas CDs.

Determination of two dimensional atmospheric trace gas distributions with high time resolution at time scales of the order of

25   seconds, i.e. fast imaging of atmospheric trace gases is possible with techniques recording all spatial pixels of an image at once

for a low number of spectral channels (see e.g. Platt et al., 2015). This allows studying phenomena which are not accessible

to conventional scanning methods. With fast trace gas imaging techniques sources and sinks of trace gases can be identified

and quantified on much smaller spatial and temporal scales than with conventional remote sensing techniques. This allows for

instance to gain insight into small scale mixing processes and to distinguish chemical conversions from transport.

30   Most of the presently used atmospheric trace gas imaging schemes either use a set of two band pass filters (e.g. SO_2 Camera,

$\sim 1\,\mathrm{Hz}$ for volcanic emissions, see e.g. Mori and Burton, 2006; Bluth et al., 2007; Kern et al., 2010; Platt et al., 2018) or a

tuneable band pass filter as wavelength selective element (e.g. NO_2 Camera, $\sim 3\,\mathrm{min}$ per image for stack emissions of power

plants Dekemper et al., 2016). These techniques either involve intricate optical set-ups with low light throughput or yield a

rather coarse spectral resolution which might result in strong cross interferences (see e.g. Lübcke et al., 2013; Kuhn et al., 2014).

Here we study the application of Fabry-Perot Interferometers (FPIs) as wavelength selective elements for trace gas imaging in the UV/Vis. The periodic FPI transmission spectrum is matched to the spectral absorption structures of trace gases that often

5 show a similar periodicity. Due to the high correlation of the transmission spectrum of the wavelength selective element and the trace gas absorption spectrum a high sensitivity can be reached and cross interferences with other absorbers are minimized, even if only a small number of spectral channels (FPI tuning settings) is used (see Kuhn et al., 2014, and the discussion in Sect. 3.2 below). Air spaced FPI etalons are very robust devices and allow for simple optical designs that can easily be implemented in imaging sensors. We present a model study on the sensitivity and selectivity of FPI Correlation Spectroscopy applied to

10 SO_2, BrO and NO_2 (Sect. 3). For exemplary measurement scenarios, we infer the possible spatio-temporal resolution of these measurements for a specific instrument implementation. We find that for the three gases imaging with spatio-temporal resolutions by around two orders of magnitude higher than state of the art methods should be possible. In addition, we present a proof of concept study of the technique for volcanic sulphur dioxide SO_2, validating the expected high accuracy and sensitivity of the technique (Sect. 4).

15 ## 2 Fabry-Perot Interferometer Correlation Spectroscopy

2.1 Fabry Perot Interferometer

The FPI is a fundamentally very simple optical device, known for more than a century (e.g. Perot and Fabry, 1899). In principle, it consists of two plane parallel surfaces each with reflectance R, separated by a distance d (see Fig. 1). The medium between the plates has the index of refraction n. Incident light (angle of incidence α) is split up in partial beams with different

20 optical path lengths between the two surfaces. Due to interference of the transmitted partial beams, the spectral transmission of the FPI is characterised by periodic transmission peaks, referring to constructive interference. For high enough orders of interference, the free spectral range (FSR) Δ_λ between two transmission peaks in units of wavelength λ is approximately given by:

$$\Delta_\lambda(\lambda) \approx \frac{\lambda^2}{2nd\cos\alpha} \qquad (2)$$

25 The finesse F of a FPI represents the ratio of FSR to the full width half maximum (FWHM) δ_λ of a transmission peak:

$$F = \frac{\Delta_\lambda}{\delta_\lambda} \qquad (3)$$

The finesse is a measure for the number of effectively interfering partial beams and therefore increasing with the surface reflectance. However, it is also depending on the alignment and quality of the surfaces.

The spectral transmission as a function of λ and the FPI's instrument parameters is given by:

30 $$T_{FPI}(\lambda) = \left[1 + \frac{4R}{(1-R)^2} \sin^2\left(\frac{2\pi dn\cos\alpha}{\lambda} \right) \right]^{-1} \qquad (4)$$

Despite its simple design, the challenge in manufacturing FPI devices lies in creating a stable set-ups keeping d stable to a fraction of a wavelength across the effective aperture.

2.2 Detection principle

The concept of using FPI correlation to detect atmospheric trace gases is described in Kuhn et al. (2014). The correlation of periodic absorption structures of atmospheric trace gases and the FPI transmission is exploited. An apparent absorbance $\tilde{\tau}_i$ of a trace gas i is calculated from the optical densities of an on-band τ_A and off-band τ_B channel:

$$\tilde{\tau}_i = \tau_A - \tau_B = \log \frac{I_{A,0}}{I_A} - \log \frac{I_{B,0}}{I_B} = (\overline{\sigma}_{A,i} - \overline{\sigma}_{B,i}) \, S_i = \Delta \overline{\sigma}_i \, S_i \tag{5}$$

S_i denotes the CD of a trace gas i. For the on-band channel, the spectral pattern of the FPI transmittance is chosen to correlate with the absorption band structure of the target trace gas, while for the off-band channel the FPI is tuned to show minimum correlation with the target trace gas absorption. The apparent absorbance is - for low trace gas optical densities - proportional to the CD of the trace gas. The proportionality is $\Delta \overline{\sigma}$, representing the difference of the effective absorption cross section seen by channel A and channel B.

In practice, a wavelength range of high correlation of spectral trace gas absorption and FPI transmission is preselected with a band pass filter (BPF). Within this spectral range the FPI physical parameters are optimised, particularly the Finesse is chosen to maximise the signal to noise ratio.

Here we apply FPI Correlation Spectroscopy for passive imaging of a trace gas in the atmosphere. This means that the light source is scattered sky radiation that is measured within an imaging FOV (e.g. 20° aperture angle). We assume in the following that a reference I_0 (i.e. a part without trace gas) is always present within the image, so that S denotes the differential trace gas CD compared to that reference.

3 Model study for SO_2, NO_2 and BrO

FPI Correlation Spectroscopy can be applied to every trace gas species that yields sufficiently strong spectral absorption structures in the regarded wavelength range. In this section we present exemplary model studies for imaging of SO_2, NO_2 and BrO. For each target trace gas we regard a typical exemplary measurement scenario (Tab. 1). For the target species BrO and SO_2 we use typical measurement scenarios of volcanic emissions in the UV spectral range. For SO_2 we assume CDs that are typically measured in volcanic plumes of a comparably weak volcanic emitter or an already highly diluted plume ($1e17$ molec cm^{-2}, see Tab. 1). We additionally chose a high and probably disturbing NO_2 CD ($1e17$ molec cm^{-2}) in oder to make the scenario also applicable to SO_2 measurements at e.g. ship or industrial stack emissions. Existing filter based SO_2 cameras are subject to strong cross interferences in this CD range (see e.g. Lübcke et al., 2013; Kuhn et al., 2014). In the scenario for BrO we assume a relatively strong but not uncommon volcanic emitter, with BrO mixing ratios of tens to hundreds ppt within the plume ($1e14$ molec cm^{-2}, see Tab. 1) and high SO_2 CDs ($3e18$ molec cm^{-2}). Gradients in the BrO distributions can give insight into in-plume halogen chemistry (see e.g. Bobrowski et al., 2007; von Glasow, 2010; Roberts et al., 2014). The NO_2

scenario (blue spectral range) is applicable to measurements of stack emissions at e.g. a coal power plant (see e.g. Dekemper et al., 2016) but also to local gradients induced by traffic ($1e16 \, \mathrm{molec \, cm^{-2}}$, see Tab. 1).

We calculate the sensitivities and study the cross interference of the apparent absorbance with other atmospheric absorbers for typical differential CDs for the respective measurement scenario. Table 1 lists the assumed differential CDs of the trace gases absorbing in the same spectral range as the trace gases under investigation. For these potentially interfering trace gases we chose relatively high values, so that the indicated cross interferences correspond to upper limits. The listed CDs represent differential CDs across a typical image FOV ($\sim 20°$), assuming that within the image always a reference region I_0 without the target trace gas is present.

In a second step, we calculate the corresponding photon budgets in order to infer the approximate achievable spatial and temporal resolution of the respective imaging measurement.

3.1 Description of the Model

The apparent absorbance is calculated from radiances I_k (in $[\mathrm{photons \, s^{-1} \, mm^{-2} \, sr^{-1}}]$) of scattered solar radiation transmitted by the respective spectral channel $k = A, B$ (on-band and off-band FPI setting) :

$$I_k = \int \mathrm{d}\lambda \, I_0(\lambda) e^{-\sum_i \sigma_i(\lambda) S_i} T_{FPI,k}(\lambda) T_{BPF}(\lambda) \tag{6}$$

A spectrum recorded at a clear day in Heidelberg with a solar zenith angle of $73°$ ($160°$ relative solar azimuth, $89°$ viewing zenith angle) was used to approximate the spectral radiance $I_0(\lambda)$. $I_0(\lambda)$ was scaled with scattered sky radiance measurements from (Blumthaler et al., 1996). The radiance measurements were performed in Innsbruck in February, 1995 with a solar zenith angle of $68°$. For our calculations we used the values for $180°$ relative solar azimuth and $70°$ viewing zenith angle. S_i is the CD of an absorbing gas species i with spectral absorption cross section $\sigma_i(\lambda)$. $T_{FPI,k}$ is the FPI transmittance in configuration k (see Eq. (4)) and T_{BPF} the transmittance of the BPF isolating the measurement wavelength range for the respective target trace gas. T_{BPF} was modeled with a higher order Gaussian function:

$$T_{BPF}(\lambda) = P e^{-\left(\frac{(\lambda_{BPF} - \lambda)^2}{2c^2}\right)^p} \tag{7}$$

with a FWHM of

$$\delta_{\lambda,BPF} = 2c\sqrt{2(\log 2)^{\frac{1}{p}}} \tag{8}$$

P describes the peak transmission at a central wavelength λ_{BPF}. An order $p = 6$ was used to approximate interference filter transmission profiles.

With Eq. (5) and the intensities I_k from Eq. (6), the apparent absorbance $\tilde{\tau}_i$ can be caluclated, allowing to study the sensitivity and selectivity of the detection of a trace gas i for given FPI instrument settings.

In addition, we approximate the respective detection limits based on photon shot noise. In order to calculate the number of photons that reach the detector of the imaging device, we need to know the etendue (product of entrance area A and aperture

solid angle Ω) of the employed optics. Kuhn et al. (2014) suggest several optical setups for FPI Correlation Spectroscopy imaging implementations. Here, we chose the setup in which, with help of an image space telecentric optics (see Fig. 5), the incident radiation from the imaging FOV is parallelised before traversing the FPI and BPF. In order to avoid strong blurring of the FPI transmission spectrum due to different incidence angles, the divergence Θ of the light beams traversing the FPI should

5   not be much larger than $\Theta = 1°$. With a lens of focal length f this condition limits the maximum aperture radius a to:

$$a = f \tan \frac{\Theta}{2} \tag{9}$$

The FPI clear aperture radius a_{FPI} determines the imaging FOV aperture angle

$$\gamma_{FOV} = 2 \arctan \frac{a_{FPI}}{f} \tag{10}$$

The etendue per pixel E_{pix} is determined by the spatial resolution of the recorded image, which can be varied by binning

10   individual pixels. For n_{pix} being the number of pixels along a column of a square detector array, the approximate etendue per pixel of the instrument is:

$$E_{pix} = A_{pix} \Omega_{pix} \approx a^2 \sin^2(\frac{\gamma_{FOV}}{2n_{pix}})\pi^2 \tag{11}$$

The detectors quantum efficiency and losses within the optics are considered to be not wavelength dependent in the regarded spectral ranges and combined in a loss factor η. We chose a somewhat lower loss factor for the UV (0.25 for SO_2 and BrO)

15   compared to the Vis (0.5 for NO_2) due to the higher quantum efficiency of commonly used detectors. Each FPI channel (on-band and off-band setting) requires one image acquisition. We assume a photon electron shot noise limited measurement, where for an exposure time Δt the number of counted photo electrons per pixel and image is

$$N_{phe,pix} = I E_{pix} \eta \Delta t \tag{12}$$

with an uncertainty of $\Delta N_{phe,pix} = \sqrt{N_{phe,pix}}$. The uncertainty in the apparent absorbance $\tilde{\tau}$ is then

20    $$\Delta \tilde{\tau} \approx \sqrt{\frac{2}{N_{phe,pix}}} \tag{13}$$

assuming the intensities I_k for the two FPI settings $k = A, B$ are similar and that the reference intensities $I_{0,k}$ have to be recorded only once.

Note, that the used sky radiances, loss factors and dimensions of the optics (see Tab. 2) represent conservative assumptions. For instance the light throughput could be enhanced by more than an order of magnitude by choosing a different optical setup (see

25   Kuhn et al., 2014). There, the FPI is placed in front of the lens using the full clear aperture and the full aperture angle of the FPI and the optics. Each viewing direction of the FOV, however, will have a different incidence angle onto the FPI and therefore a different FPI transmission spectrum, which has to be accounted for in the data analysis. Alternatively, simply a larger FPI could be used. The results of the following calculations for the image space telecentric optics, therefore, represent lower limits of the performance.

3.2 Results of the simulations

The FPI Correlation Spectroscopy technique allows for numerous different realisations regarding the used spectral window and FPI instrument parameters that can be chosen according to e.g. measurement conditions or availability of optical components (FPI, BPF). Here, we identified spectral windows in which the target trace gas absorption cross sections exhibit approximately

5 periodic structure and appropriate FPI parameters were determined in order to maximise the correlation of FPI transmission and trace gas absorption according to the procedures described in Kuhn et al. (2014). Table 2 lists the parameters for the exemplary setups we use in this work.

The results for SO_2, BrO and NO_2 are summarized in Fig. 2, 3 and 4, which show the differential optical densities of the target trace gas and the potentially interfering trace gases for the respective measurement wavelength ranges (panels a). In the

10 lower panels, the transmitted spectral radiances of the respective FPI spectral channels (on-band, off-band) are plotted. The SO_2 and NO_2 trace gas optical density clearly dominate the total differential optical density for the targeted detection limits. For BrO the other trace gases exhibit differential optical depths on the same order of magnitude as BrO. In the b) panels of the same figures, the respective simulated calibration curves are plotted, where the dashed lines indicate the impact of the individual interferring gases for the assumed amounts. For all three gases these impacts are well below the targeted detection

15 limit. Especially for the case of BrO this illustrates, how FPI Correlation Spectroscopy can effectively separate the absorption structure of a single trace gas from a multitude of trace gas optical densities of the same order of magnitude. By using more than two FPI settings, the selectivity can be enhanced even further.

Table 3 summarises the results of the photon budget calculations. We calculated the maximum possible spatial resolution of the imaging measurement for a $10\,s$ exposure time and the instrument parameters listed in Tab. 2. For this, spatial pixels are

20 co-added until the targeted detection limit was reached. We find that for the targeted detection limits the spatial resolutions of the imaging measurements for the chosen parameters are 226 by 226 pixels for SO_2, 51 by 51 pixels for BrO and 252 by 252 pixels for NO_2 for a temporal resolution of 10 s. The temporal resolution could be enhanced at the expense of the spatial resolution or vice versa. For instance, cutting the linear spatial resolution in half (e.g. from 226 by 226 to 113 by 113 pixels for SO_2), would reduce the temporal resolution to 5s for the same detection limit.

25 When comparing to corresponding DOAS measurements the enormous increase of spatio-temporal resolution becomes evident. A state of the art DOAS measurement takes around $1\,s$ to reach a detection limit of $1 \cdot 10^{14}\,molec\,cm^{-2}$ BrO for one spatial pixel. To scan the ca. 2600 pixels of the assumed BrO image would take 2600s. An imaging DOAS instrument (e.g. Lohberger et al., 2004) does simplify the scanning process but will not improve the light budget. Our results show that FPI Correlation Spectroscopy can be more than two orders of magnitude faster than a DOAS measurement while maintaining a similar degree

30 of selectivity and interference suppression.

The presented results of the exemplary calculations for SO_2, BrO and NO_2 suggest that FPI Correlation Spectroscopy can also be implemented for other trace gases with similarly strong and structured absorption, such as e.g. O_3, HCHO, IO, or OClO.

4 Proof of concept: Field measurements of volcanic SO$_2$

The above model study on trace gas detection with FPI Correlation Spectroscopy was validated in a proof of concept field study for volcanic SO$_2$. In a one-pixel prototype a single photodiode was used as detector. A BPF ($\lambda_{BPF} \approx 310\,\mathrm{nm}, \delta_{\lambda,BPF} \approx 10\,\mathrm{nm}$) was used for the preselection of a wavelength range, where the SO$_2$ differential absorption is strong and approximately

5   periodic. A FPI (air-spaced etalon from *SLS Optics Ltd.*) with a FSR of 2.1 nm and a Finesse of 7 across a clear aperture of 20 mm was tilted by a servo motor in order to tune it to the on-band and off-band transmission settings. The individual plates of the FPI have a finite thickness and two surfaces, the outer surfaces have an anti-reflective coating and are slightly wedged from the inner surfaces of the plates, so their influence can be neglected here. The optical setup behind FPI and BPF consists of a fused silica lens ($f = 50\,\mathrm{mm}$), which projects light from a narrow FOV ($\sim 0.8°$ aperture angle) onto the photodiode.

10 Radiances for the on-band and off-band channel were recorded, delivering an apparent absorbance measurement with 0.42 Hz. A telescope ($\sim 0.5°$ aperture angle) was co aligned with the one pixel FPI setup and connected to a temperature stabilized spectrometer (spectral resolution $\sim 0.8\,\mathrm{nm}$). The recorded spectra ($\sim 0.13\,\mathrm{Hz}$) were evaluated with the DOAS algorithm. The measurement was performed at the *Osservatorio Vulcanologico Pizzi Deneri* (37.766° N, 15.017° E) at Mt. Etna on Sicily on the 30 July 2017. The device was pointed towards the volcanic plume of Mt. Etna with constant viewing angle (8° viewing

15 elevation, azimuth 280° N). A plume free part of the sky was used for reference measurements. Fig. 6 shows the time series of the apparent absorbance of the FPI Correlation Spectroscopy prototype together with the SO$_2$ CD retrieved from the co-recorded spectra. The apparent absorbance shows high correlation with the retrieved SO$_2$ CD. In Fig. 7 the correlation plot is shown. For high SO$_2$ CDs the sensitivity of $\tilde{\tau}_{SO_2}$ decreases slightly due to saturation effects. A simulation for the used instrument configuration (differing only by $\lambda_{BPF} = 310\,\mathrm{nm}$ from the above simulation) reproduces the recorded calibration

20 curve well. The remaining scatter of the values mainly originates from slight misalignment and the difference of the two narrow FOVs.

The recorded UV spectra also allow for evaluating the O$_3$ absorption. The lower panel of Fig. 6 shows the change of the differential O$_3$ CD during the measurement with respect to the reference. The observed increase of the O$_3$ CD by more then $4 \cdot 10^{18}\,\mathrm{molec\,cm^{-2}}$ is due to the increasing stratospheric light path with increasing solar zenith angle (63.58° to 79.31° during

25 the measurement sequence). Within an imaging FOV (of e.g. 17°) much lower differential O$_3$ CDs are expected (see Tab. 2), since all pixels are similarly affected by the change in O$_3$ background. Even with this extreme change in O$_3$ CD no impact on the recorded SO$_2$ apparent absorbances is observed.

The one pixel prototype can be implemented in a full frame imaging instrument with e.g. the image space telecentric optical setup, used for the above calculations and shown in Fig. 5. In principle, the single pixel detector (photodiode) is replaced by

30 a two dimensional detector array (UV sensitive for SO$_2$ and BrO) and an aperture stop is added in the focal plane in front of the lens. This would, however, reduce the light throughput per pixel of the imaging setup compared to the one pixel prototype. Alternatively, the FPI could be placed in front of the lens using the full clear aperture and the full aperture angle of the FPI and the optics (see Kuhn et al., 2014). This leads to a much higher light throughput, however, the incidence angle of the incident light onto the FPI and thereby the FPI transmission spectrum becomes dependent on the pixel (i.e. the viewing direction within

the imaging FOV) and has to be accounted for in the data evaluation.

The data of the field study also indicate the potential of using an additional DOAS measurement for the absolute calibration of the apparent absorbance. The position of the narrow FOV of a DOAS telescope pointing into the wide imaging FOV can be retrieved from time series and used for an in-operation calibration as in the case of the SO2-camera (see e.g. Sihler et al., 2017; Lübcke et al., 2013).

5   Conclusions

Many locally variable atmospheric processes are difficult to quantify with state of the art UV/Vis remote sensing methods (e.g. DOAS) due to the limited spatio-temporal resolution. This makes it difficult to e.g. quantify the emission of point sources or to separate the effects of transport and chemical conversion on local scales. Kuhn et al. (2014) proposed the FPI Correlation Spectroscopy for SO_2 in the UV wavelength range after similar approaches have been studied in infrared wavelength ranges (e.g. Wilson et al., 2007; Vargas-Rodríguez and Rutt, 2009). The major motivation is to reduce the number of spectral channels used for the trace gas detection in order to increase the spatio-temporal resolution of the measurement while maintaining its selectivity.

In a model study we investigated the sensitivity and determined the photon budget of FPI Correlation Spectroscopy for three measurement scenarios for SO_2, BrO and NO_2. For SO_2 we assumed a scenario with rather low volcanic emissions, which is also representative for industrial stack or ship emissions. For BrO a scenario with stronger volcanic emissions was assumed, with BrO mixing ratios of 10 to 100 ppt within the volcanic plume and high SO_2 CDs. The NO_2 measurement scenario represents typical stack emissions of power plants and gradients of local air pollution induced by e.g. traffic.

For all three investigated gases, cross interferences with other trace gases absorbing in the preselected spectral ranges were found to be very low, meaning that the selectivity of FPI Correlation Spectroscopy can be similar to the selectivity of conventional techniques (e.g. DOAS). In this study, we only used two FPI settings. A larger number of FPI settings could be used to further reduce possible cross interferences.

Using rather conservative assumptions regarding the intensity of the incoming radiation and the size of the instrument optics, we calculated the highest possible spatio-temporal resolution of the FPI Correlation Spectroscopy measurements for the different scenarios and found that they can be more than two orders of magnitude higher compared to state of the art DOAS measurements for the same trace gas CD. This means that in the same time period a conventional dispersive technique records a single viewing direction (i.e. a single spatial pixel), almost an entire image can be recorded with the FPI Correlation Spectroscopy. This strongly indicates that future instruments based on FPI Correlation Spectroscopy can provide unprecedented insight into short time or small scale processes in the atmosphere.

In the second part, we presented a proof of concept field study for FPI Correlation Spectroscopy applied to volcanic SO_2, which confirms the model simulations by comparing the measured apparent absorbance to SO_2 CDs retrieved by a co-aligned DOAS measurement. One particularly important finding is that, as expected from the model study, no O_3 cross interference can be observed over a large O_3 CD range.

The extension of the one pixel prototype to a camera can be accomplished comparably easily by minor modifications of the optics and by using a UV sensitive detector array and should be the aim of future studies. By replacing the FPI and the BPF, the instrument is adjusted to measure different trace gases, e.g. BrO and NO_2 according to the model calculations performed in Sect. 3. A co-aligned narrow FOV DOAS measurement can be used for an in-operation calibration of the recorded apparent

5   absobance images.

The applications of UV/Vis FPI Correlation Spectroscopy mentioned in this work represent only some examples for and trace gases and phenomena that could be studied. Beyond the volcanological application, FPI imaging can for instance be used to study SO_2 in air pollution or BrO in salt pans (see e.g. Holla et al., 2015). The technique can also be applied to other trace gases with similarly strong and structured absorption, such as e.g. O_3, HCHO, IO, or OClO.

10   *Data availability.*   The data used for the proof of concept study can be obtained from the authors upon request.

Competing interests.   The authors declare that they have no conflict of interest.

Acknowledgements.   We would like to thank *SLS Optics Ltd.* for sharing their expertise in designing and manufacturing etalons.

References

Blumthaler, M., Gröbner, J., Huber, M., and Ambach, W.: Measuring spectral and spatial variations of UVA and UVB sky radiance, Geophysical Research Letters, 23, 547–550, https://doi.org/10.1029/96gl00248, 1996.

Bluth, G., Shannon, J., Watson, I., Prata, A., and Realmuto, V.: Development of an ultra-violet digital camera for volcanic SO2 imaging, Journal of Volcanology and Geothermal Research, 161, 47–56, 2007.

Bobrowski, N. and Giuffrida, G.: Bromine monoxide/sulphur dioxide ratios in relation to volcanological observations at Mt. Etna 2006-2009, Solid Earth, 3, 433, 2012.

Bobrowski, N., von Glasow, R., Aiuppa, A., Inguaggiato, S., Louban, I., Ibrahim, O. W., and Platt, U.: Reactive halogen chemistry in volcanic plumes, J. Geophys. Res., 112, D06 311, https://doi.org/10.1029/2006JD007206, http://dx.doi.org/10.1029/2006JD007206, 2007.

Bogumil, K., Orphal, J., Homann, T., Voigt, S., Spietz, P., Fleischmann, O., Vogel, A., Hartmann, M., Kromminga, H., Bovensmann, H., Frerick, J., and Burrows, J.: Measurements of molecular absorption spectra with the {SCIAMACHY} pre-flight model: instrument characterization and reference data for atmospheric remote-sensing in the 230-2380 nm region, Journal of Photochemistry and Photobiology A: Chemistry, 157, 167 – 184, https://doi.org/http://dx.doi.org/10.1016/S1010-6030(03)00062-5, http://www.sciencedirect.com/science/article/pii/S1010603003000625, atmospheric Photochemistry, 2003.

Chance, K. and Orphal, J.: Revised ultraviolet absorption cross sections of H2CO for the HITRAN database, Journal of Quantitative Spectroscopy and Radiative Transfer, 112, 1509–1510, https://doi.org/10.1016/j.jqsrt.2011.02.002, 2011.

Dekemper, E., Vanhamel, J., Van Opstal, B., and Fussen, D.: The AOTF-based NO 2 camera, Atmospheric Measurement Techniques, 9, 6025, 2016.

Fleischmann, O. C., Hartmann, M., Burrows, J. P., and Orphal, J.: New ultraviolet absorption cross-sections of BrO at atmospheric temperatures measured by time-windowing Fourier transform spectroscopy, Journal of Photochemistry and Photobiology A: Chemistry, 168, 117 – 132, https://doi.org/http://dx.doi.org/10.1016/j.jphotochem.2004.03.026, http://www.sciencedirect.com/science/article/pii/S1010603004001522, 2004.

Gliß, J., Bobrowski, N., Vogel, L., Pöhler, D., and Platt, U.: OClO and BrO observations in the volcanic plume of Mt. Etna and implications on the chemistry of chlorine and bromine species in volcanic plumes, Atmospheric Chemistry and Physics, 15, 5659–5681, https://doi.org/10.5194/acp-15-5659-2015, http://www.atmos-chem-phys.net/15/5659/2015/, 2015.

Holla, R., Schmitt, S., Frieß, U., Pöhler, D., Zingler, J., Corsmeier, U., and Platt, U.: Vertical distribution of BrO in the boundary layer at the Dead Sea, Environmental Chemistry, 12, 438–460, https://doi.org/10.1071/EN14224, http://dx.doi.org/10.1071/EN14224, 2015.

Hönninger, G., von Friedeburg, C., and Platt, U.: Multi axis differential optical absorption spectroscopy (MAX-DOAS), Atmos. Chem. Phys., 4, 231–254, https://doi.org/10.5194/acp-4-231-2004, http://www.atmos-chem-phys.net/4/231/2004/, 2004.

Kern, C., Kick, F., Lübcke, P., Vogel, L., Wöhrbach, M., and Platt, U.: Theoretical description of functionality, applications, and limitations of SO_2 cameras for the remote sensing of volcanic plumes, Atmos. Meas. Tech., 3, 733–749, https://doi.org/10.5194/amt-3-733-2010, http://www.atmos-meas-tech.net/3/733/2010/, 2010.

Kromminga, H., Orphal, J., Spietz, P., Voigt, S., and Burrows, J. P.: New measurements of OClO absorption cross-sections in the 325-435 nm region and their temperature dependence between 213 and 293 K, Journal of Photochemistry and Photobiology A: Chemistry, 157, 149–160, https://doi.org/10.1016/S1010-6030(03)00071-6, http://www.sciencedirect.com/science/article/pii/S1010603003000716, 2003.

Kuhn, J., Bobrowski, N., Lübcke, P., Vogel, L., and Platt, U.: A Fabry Perot interferometer-based camera for two-dimensional mapping of SO_2 distributions, Atmospheric Measurement Techniques, 7, 3705–3715, https://doi.org/10.5194/amt-7-3705-2014, http://www.atmos-meas-tech.net/7/3705/2014/, 2014.

Lohberger, F., Hönninger, G., and Platt, U.: Ground-Based Imaging Differential Optical Absorption Spectroscopy of Atmospheric Gases, Appl. Opt., 43, 4711–4717, https://doi.org/10.1364/AO.43.004711, http://ao.osa.org/abstract.cfm?URI=ao-43-24-4711, 2004.

Lübcke, P., Bobrowski, N., Illing, S., Kern, C., Nieves, J. M. A., Vogel, L., Zielcke, J., Granados, H. D., and Platt, U.: On the absolute calibration of SO2 cameras, Atmospheric Measurement Techniques, 6, 677–696, https://doi.org/10.5194/amt-6-677-2013, 2013.

Mori, T. and Burton, M.: The SO2 camera: A simple, fast and cheap method for ground-based imaging of SO2 in volcanic plumes, Geophysical Research Letters, 33, 2006.

Perot, A. and Fabry, C.: On the Application of Interference Phenomena to the Solution of Various Problems of Spectroscopy and Metrology, The Astrophysical Journal, 9, 87, https://doi.org/10.1086/140557, 1899.

Platt, U. and Stutz, J.: Differential optical absorption spectroscopy, Springer Verlag, 2008.

Platt, U., Lübcke, P., Kuhn, J., Bobrowski, N., Prata, F., Burton, M., and Kern, C.: Quantitative imaging of volcanic plumes - Results, needs, and future trends, Journal of Volcanology and Geothermal Research, 300, 7–21, 2015.

Platt, U., Bobrowski, N., and Butz, A.: Ground-Based Remote Sensing and Imaging of Volcanic Gases and Quantitative Determination of Multi-Species Emission Fluxes, Geosciences, 8, 44, https://doi.org/10.3390/geosciences8020044, 2018.

Roberts, T., Martin, R., and Jourdain, L.: Reactive bromine chemistry in Mount Etna's volcanic plume: the influence of total Br, high-temperature processing, aerosol loading and plume–air mixing, Atmospheric Chemistry and Physics, 14, 11 201–11 219, 2014.

Roscoe, H. K., Van Roozendael, M., Fayt, C., du Piesanie, A., Abuhassan, N., Adams, C., Akrami, M., Cede, A., Chong, J., Clémer, K., Friess, U., Gil Ojeda, M., Goutail, F., Graves, R., Griesfeller, A., Grossmann, K., Hemerijckx, G., Hendrick, F., Herman, J., Hermans, C., Irie, H., Johnston, P. V., Kanaya, Y., Kreher, K., Leigh, R., Merlaud, A., Mount, G. H., Navarro, M., Oetjen, H., Pazmino, A., Perez-Camacho, M., Peters, E., Pinardi, G., Puentedura, O., Richter, A., Schönhardt, A., Shaiganfar, R., Spinei, E., Strong, K., Takashima, H., Vlemmix, T., Vrekoussis, M., Wagner, T., Wittrock, F., Yela, M., Yilmaz, S., Boersma, F., Hains, J., Kroon, M., Piters, A., and Kim, Y. J.: Intercomparison of slant column measurements of NO_2 and O_4 by MAX-DOAS and zenith-sky UV and visible spectrometers, Atmos. Meas. Tech., 3, 1629–1646, https://doi.org/10.5194/amt-3-1629-2010, http://www.atmos-meas-tech.net/3/1629/2010/, 2010.

Rothman, L., Gordon, I., Babikov, Y., Barbe, A., Benner, D. C., Bernath, P., Birk, M., Bizzocchi, L., Boudon, V., Brown, L., Campargue, A., Chance, K., Cohen, E., Coudert, L., Devi, V., Drouin, B., Fayt, A., Flaud, J.-M., Gamache, R., Harrison, J., Hartmann, J.-M., Hill, C., Hodges, J., Jacquemart, D., Jolly, A., Lamouroux, J., Roy, R. L., Li, G., Long, D., Lyulin, O., Mackie, C., Massie, S., Mikhailenko, S., Müller, H., Naumenko, O., Nikitin, A., Orphal, J., Perevalov, V., Perrin, A., Polovtseva, E., Richard, C., Smith, M., Starikova, E., Sung, K., Tashkun, S., Tennyson, J., Toon, G., Tyuterev, V., and Wagner, G.: The {HITRAN2012} molecular spectroscopic database, Journal of Quantitative Spectroscopy and Radiative Transfer, 130, 4 – 50, https://doi.org/http://dx.doi.org/10.1016/j.jqsrt.2013.07.002, http://www.sciencedirect.com/science/article/pii/S0022407313002859, {HITRAN2012} special issue, 2013.

Serdyuchenko, A., Gorshelev, V., Weber, M., Chehade, W., and Burrows, J. P.: High spectral resolution ozone absorption cross-sections - Part 2: Temperature dependence, Atmos. Meas. Tech., 7, 625–636, https://doi.org/10.5194/amt-7-625-2014, http://www.atmos-meas-tech.net/7/625/2014/, 2014.

Sihler, H., Lübcke, P., Lang, R., Beirle, S., de Graaf, M., Hörmann, C., Lampel, J., de Vries, M. P., Remmers, J., Trollope, E., Wang, Y., and Wagner, T.: In-operation field-of-view retrieval (IFR) for satellite and ground-based DOAS-type instruments applying coincident high-resolution imager data, Atmospheric Measurement Techniques, 10, 881–903, https://doi.org/10.5194/amt-10-881-2017, 2017.

Thalman, R. and Volkamer, R.: Temperature dependent absorption cross-sections of O_2-O_2 collision pairs between 340 and 630 nm and at atmospherically relevant pressure, Phys. Chem. Chem. Phys., 15, 15 371–15 381, https://doi.org/10.1039/C3CP50968K, http://dx.doi.org/10.1039/C3CP50968K, 2013.

Vandaele, A. C., Hermans, C., and Fally, S.: Fourier transform measurements of SO 2 absorption cross sections: II.: Temperature dependence in the 29000–44000cm- 1 (227–345nm) region, Journal of Quantitative Spectroscopy and Radiative Transfer, 110, 2115–2126, 2009.

Vargas-Rodríguez, E. and Rutt, H.: Design of CO, CO2 and CH4 gas sensors based on correlation spectroscopy using a Fabry–Perot interferometer, Sensors and Actuators B: Chemical, 137, 410–419, https://doi.org/10.1016/j.snb.2009.01.013, 2009.

von Glasow, R.: Atmospheric chemistry in volcanic plumes, Proceedings of the National Academy of Sciences, 107, 6594–6599, 2010.

Wilson, E. L., Georgieva, E. M., and Heaps, W. S.: Development of a Fabry–Perot interferometer for ultra-precise measurements of column CO2, Measurement Science and Technology, 18, 1495–1502, https://doi.org/10.1088/0957-0233/18/5/040, 2007.
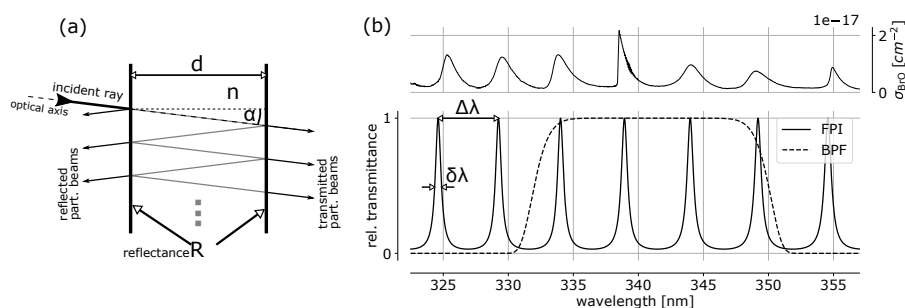
Figure 1. (a) FPI schematics indicating the splitting of incident radiation into partial beams that interfere to cause the FPI transmittance spectrum (b), which is characterised by periodic transmission maxima with a FWHM of δ_λ and a FSR of Δ_λ. The BrO absorption cross section (upper panel) shows approximately periodic structures allowing for a high correlation with spectral FPI transmittance.
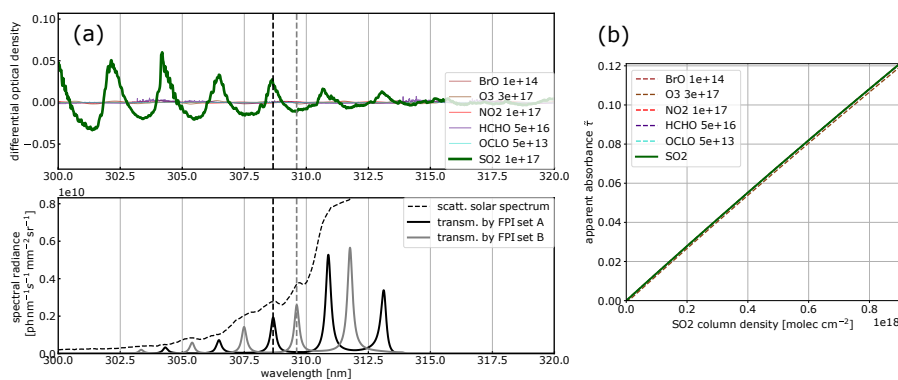
Figure 2. Model results for SO_2: (a) the differential optical densities of the assumed differential trage gas CDs are plotted in the upper panel. The lower panel shows the spectral radiance of the sky (dashed line) and the transmitted spectral radiances of the FPI and BPF (drawn lines, on-band in black, off-band in gray). (b) shows the calculated calibration curve for SO_2 only (drawn line) and with different interfering species included (dashed lines, CDs in $[\mathrm{molec\,cm^{-2}}]$ see legend and Tab. 1).
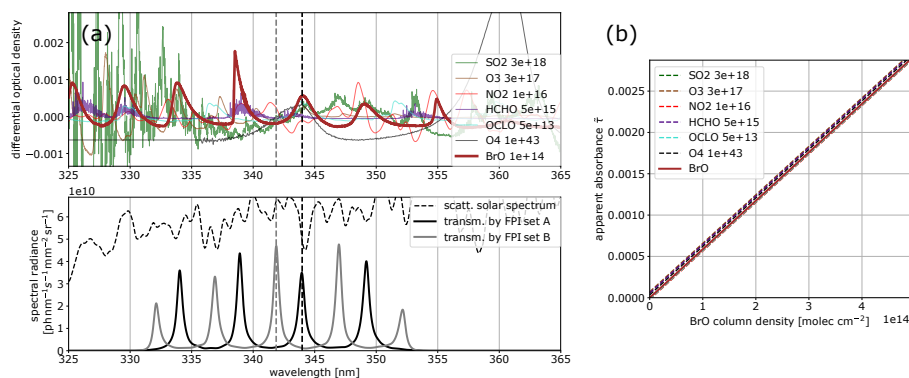
Figure 3. Model results for BrO: (a) the differential optical densities of the assumed differential trage gas CDs are plotted in the upper panel. The lower panel shows the spectral radiance of the sky (dashed line) and the transmitted spectral radiances of the FPI and BPF (drawn lines, on-band in black, off-band in gray). (b) shows the calculated calibration curve for BrO only (drawn line) and with different interfering species included (dashed lines, CDs in $[\mathrm{molec\,cm^{-2}}]$ see legend and Tab. 1).
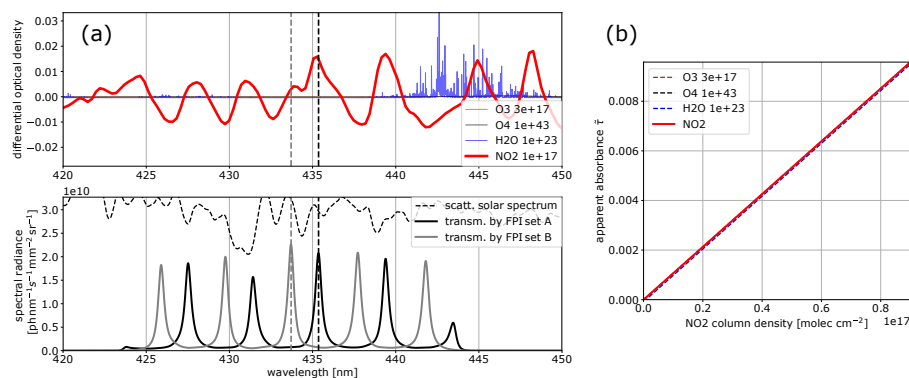
Figure 4. Model results for NO$_2$: (a) the differential optical densities of the assumed differential trage gas CDs are plotted in the upper panel. The lower panel shows the spectral radiance of the sky (dashed line) and the transmitted spectral radiances of the FPI and BPF (drawn lines, on-band in black, off-band in gray). (b) shows the calculated calibration curve for NO$_2$ only (drawn line) and with different interfering species included (dashed lines, CDs in $[\mathrm{molec\,cm^{-2}}]$ see legend and Tab. 1).
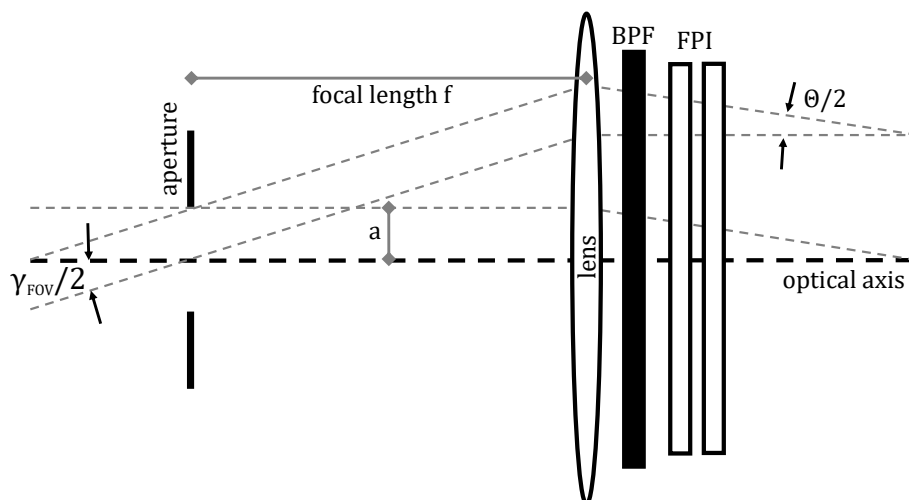
Figure 5. Image space telecentric optical setup for parallelising light from the imaging FOV before traversing the FPI and BPF.
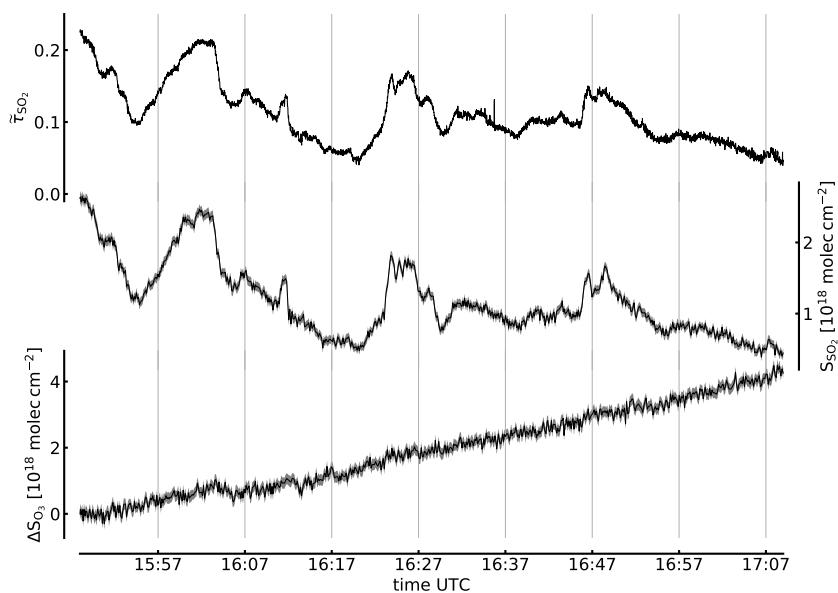
Figure 6. Time series of the apparent absorbance of the one pixel FPI Correlation Spectroscopy prototype for SO_2 detection (top trace, left scale) recorded at Etna, Sicily on 30 July 2017. A co-aligned telescope was used to simultaneously record spectra for DOAS evaluation of SO_2 and O_3 (center and bottom traces and right and bottom left scales, respectively). The apparent absorbance nicely correlates with the SO_2 CD (see Fig. 7), while no O_3 impact is observable. The growth of the retrieved O_3 differential CD is expected due to the increasing stratospheric O_3 column for increasing solar zenith angle (see text).
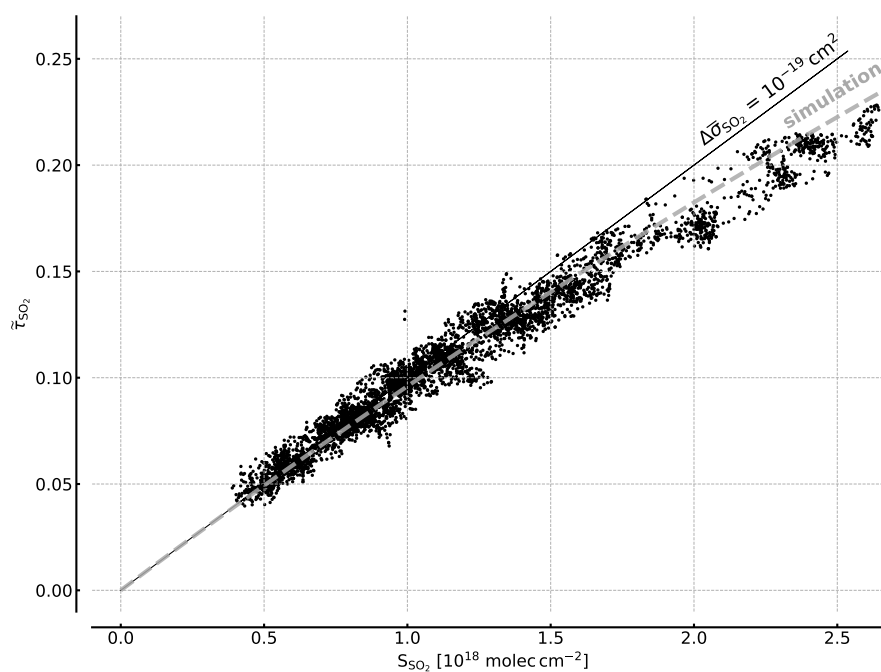
Figure 7. Correlation plot of the recorded FPI Correlation Spectroscopy apparent absorbance and the SO_2 CD retrieved by DOAS. A sensitivity of $\Delta\overline{\sigma}_{SO_2}$ of $10^{-19}\,\mathrm{cm}^2$ is reached for lower SO_2 CDs. For higher CDs a flattening of the curve is observed that is induced by saturation effects due to the high SO_2 optical densities at the absorption peaks. Also the simulation (as in Sect. 3 and Fig. 2 but with $\lambda_{BPF} = 10\,\mathrm{nm}$) reproduces the measurement very well.

Table 1. Differential CDs assumed for the different measurement scenarios. The values represent high values for CD variations within a typ. imaging FOV. The targeted detection limits are indicated in bold face.

	differential CD across imaging FOV [molec cm^{-2}]		
	SO$_2$: volcanic emission (low) 300 - 315nm	BrO: volcanic emission (high) 330 - 355nm	NO$_2$: stack emission 424 - 445nm
SO$_2$	**1e17** (volcanic)	3e18 (volcanic)	-
BrO	1e14 (volcanic)	**1e14** (volcanic)	-
NO$_2$	1e16 (bgr. pollution)	1e16 (bgr. pollution)	**1e16** (stack plume)
O$_3$	3e17 (SZA change strat.)	3e17 (SZA change strat.)	3e17 (SZA change strat.)
HCHO	5e15 (background)	5e15 (background)	-
H$_2$O	-	-	1e23 (background)
OClO	5e13 (volcanic)	5e13 (volcanic)	-
O$_4$	-	1e43 (O$_2$ dimer, [molec^{2}cm^{-5}])	1e43 (O$_2$ dimer, [molec^{2}cm^{-5}]))

typical values based on: Roscoe et al. (2010); Gliß et al. (2015); Bobrowski and Giuffrida (2012); Dekemper et al. (2016); absorption cross sections: Vandaele et al. (2009); Fleischmann et al. (2004); Bogumil et al. (2003); Serdyuchenko et al. (2014); Chance and Orphal (2011); Rothman et al. (2013); Kromminga et al. (2003); Thalman and Volkamer (2013)

Table 2. Instrument parameters of FPI, BPF and optical setup used for the simulations. The radiance for the on-band setting I_A at the detector was approximated based on the instrument parameters and sky radiance values from Blumthaler et al. (1996).

	instrument parameters			
	SO$_2$	BrO	NO$_2$	
d_A [μm]	21.60	11.52	23.72	FPI surface displacement setting A
d_B [μm]	21.44	11.62	23.63	FPI surface displacement setting B
R	0.7	0.7	0.7	FPI surface reflectivity
P_{BPF}	0.7	0.7	0.7	BPF peak transmission
λ_{BPF} [nm]	308	342	434	BPF central wavelength
$\delta_{\lambda,BPF}$ [nm]	10	20	18	BPF FWHM
f [mm]		50		focal length of imaging optics
Θ [°]		1		required parallelisation
a [mm]		0.44		aperture radius of imaging optics
a_{FPI} [mm]		7.5		aperture radius of FPI
η	0.25		0.5	loss factor
γ_{FOV} [°]		17		imaging FOV of camera
I_A [photons s^{-1} mm^{-2} sr^{-1}]	4.51e9	1.48e11	5.17e11	

Table 3. Simulation results: the spatial resolution of a FPI Correlation Spectroscopy measurement was calculated for an exposure time of $10\,\mathrm{s}$ and the target detection limits, shown in Tab. 1.

	simulation results		
	SO_2	BrO	NO_2
$\Delta\overline{\sigma}\ [\mathrm{cm^{-2}}]$	1.5e-19	6e-18	1.1e-19
target det. lim. $[\mathrm{molec\,cm^{-2}}]$	1e17	1e14	1e16
target det. lim $\tilde{\tau}$	0.015	0.0006	0.0011
required $N_{phe,pix}$	8.9e3	5.6e6	1.7e6
required $E_{pix}\ [\mathrm{mm^2\,sr}]$	7.9e-7	1.5e-5	6.6e-7
max. spatial resolution ($n_{pix} \times n_{pix}$)	**226×226**	**51×51**	**252×252**